Contents lists available at ScienceDirect

Earth and Planetary Science Letters

Plate motion in sheared granular fault system

Ke Gao [a,b,*], Robert A. Guyer [b,c], Esteban Rougier [b], Paul A. Johnson [b]

[a] *Department of Earth and Space Sciences, Southern University of Science and Technology, Shenzhen 518055, Guangdong, China*
[b] *Geophysics, Los Alamos National Laboratory, Los Alamos 87545, NM, USA*
[c] *Department of Physics, University of Nevada, Reno 89557, NV, USA*

ARTICLE INFO

ABSTRACT

Plate motion near the fault gouge layer, and the elastic interplay between the gouge layer and the plate under stick-slip conditions, is key to understanding the dynamics of sheared granular fault systems. Here, a two-dimensional implementation of the combined finite-discrete element method (FDEM), which merges the finite element method (FEM) and the discrete element method (DEM), is used to explicitly simulate a sheared granular gouge fault system. We focus on investigating the influence of normal load, driving shear velocity and plate stiffness on the velocities and displacements in the direction parallel to the shear direction (x-direction) measured at locations on the upper and lower plates just adjacent to the gouge. The simulations show that during slip phases the magnitudes of the measured velocities on the upper and lower plates are proportional to the normal load and may be inversely proportional to the square root of the plate's shear modulus. Whereas, the driving shear velocity does not show distinct influence on the measured velocities. Additionally, large slip velocities are generally associated with large macroscopic friction coefficient drops. For the models subjected to smaller normal loads, larger shear velocities and with stiffer shear plates, the same magnitude of slip velocity could cause a larger drop of macroscopic friction coefficient. During stick phases, the velocities of the upper and lower plates are respectively slightly greater and slightly smaller than half of the driving shear velocity and are both in the same direction of shear. The shear strain rate of the gouge is calculated from this velocity difference between the upper and lower plate during stick phases and thus the gouge effective shear modulus can be calculated. The results show that the gouge effective shear modulus increases proportionally with normal load, while the influence of shear velocity and plate stiffness on gouge effective shear modulus is minor. The simulations address the dynamics of a laboratory-scale fault gouge system and may aid in revealing the complexities of earthquake frictional dynamics.

1. Introduction

The nucleation and growth of earthquakes are driven by fault friction. A better understanding of friction would therefore advance dynamical modeling of earthquakes. The fault gouge, an ensemble of solid granular particles created by comminution – the fragmentation and wearing of fault blocks – plays a key role in the frictional stability of a fault (Dorostkar et al., 2017b; Marone et al., 1990). Therefore, stick-slip cycles (or simply stick-slip) in sheared granular fault systems have been intensively studied in recent years both in laboratory experiments and numerical simulations (e.g., Gao et al., 2018; Geller et al., 2015; Johnson and Jia, 2005; Johnson et al., 2008; Marone, 1998; Marone et al., 1990; Scuderi et al., 2017a). In these studies, the model employed generally consists of granular gouge compressed and sheared by confining plates which play the role of fault blocks. However, significant attention has been paid to gouge kinematics and dynamics, with few details being reported regarding the motion of the plates, especially adjacent to the gouge. This near-gouge interaction with plate motion not only directly controls the output of acoustic signals that may serve as harbingers for stick-slip events, but also reflects the physical and dynamic properties of the fault system such as the laboratory equivalence of seismic moment and characteristics of the radiated acoustic waves (Gao et al., 2019; Jackson and McKenzie, 1988; Johnson et al., 2013; Rivière et al., 2018; Rouet-Leduc et al., 2018, 2017; Siman-Tov and Brodsky, 2018; Taylor and Brodsky, 2019). Therefore, investigating stick-slip induced near gouge plate motion in sheared granular fault system is key to improving our understanding of the complex mechanisms of fault friction and may also shed light on the scale of ground motion and earthquake hazard.

* Corresponding author at: Department of Earth and Space Sciences, Southern University of Science and Technology, Shenzhen 518055, Guangdong, China.
E-mail address: gaok@sustech.edu.cn (K. Gao).

Numerical simulation is widely used to model single fault or fault patches simply because of its ease of implementation and capability of analyzing a granular gouge fault system at a level of spatial and temporal resolution not accessible experimentally (de Arcangelis et al., 2011). Among the many numerical methods available, the discrete element method (DEM) has been the most widely applied (e.g., Dorostkar et al., 2017a, 2017b; Ferdowsi et al., 2013; Griffa et al., 2011; Mair and Hazzard, 2007; Wang et al., 2017). In classic DEM models, the granular fault gouge is commonly represented by a pack of rigid particles, and the representation of the confining plates is simplified by a set of bonded particles (Abe and Mair, 2005; Dorostkar et al., 2017b; Ferdowsi et al., 2014; Griffa et al., 2013; Mair and Abe, 2008) (e.g., Fig. S1a of the Supplementary Material). As a result, by using DEM it is challenging to capture detailed deformation and motion within both the particles and plates (Dratt and Katterfeld, 2017; Ma et al., 2016). In particular, in DEM models, because the shearing plates behave as rigid bodies, the spatial variation of plate motion along the gouge in response to stick-slip cycles is difficult to acquire.

From a computational mechanics viewpoint, a granular fault system is essentially a combination of continua (each individual plate and particle) and discontinua (particle-particle and particle-plate interactions). Considering this, a numerical tool such as the combined finite-discrete element method (FDEM) (Munjiza, 1992, 2004; Munjiza et al., 2011, 2014), which merges finite element based analysis of continua with discrete element based analysis of discontinua, provides a natural solution for such a problem. In an FDEM realization of the granular fault system (Fig. S1b), each plate and each particle are represented by discrete elements, which provide the means for tracking of their motion and interactions with neighboring objects. Furthermore, each discrete element is discretized into finite elements allowing for describing its deformation in response to external forces. Therefore, by utilizing FDEM one can obtain an explicit representation of a granular fault system and thus be capable of obtaining detailed information regarding internal gouge behavior and gouge-plate motion during the full stick-slip cycle.

In this paper, based on the FDEM simulations of a granular fault system, we explore the motion of the gouge and plates during multiple stick-slip cycles. This analysis is conducted for models featuring different plate stiffness and subjected to different normal loads and shear velocities. We first provide a brief introduction to the numerical method including the theory of FDEM and model setup. Then the motion of both the upper and lower plates in stick and slip phases in terms of velocity and displacement in directions parallel to the shear direction (*x*-direction) are analyzed. The influence of normal load, shear velocity and plate stiffness on the plate motion is demonstrated and the gouge effective shear modulus interpreted from the plate motion is presented. We discuss a possible scaling relationship for the plate motion and gouge effective shear modulus with respect to normal load, shear velocity and plate stiffness and conclude.

2. Numerical methods

2.1. FDEM in a nutshell

The FDEM was originally developed by Munjiza in the early 1990s to simulate the material transition from continuum to discontinuum (Munjiza, 1992). The essence of this method is to merge the algorithmic advantages of DEM with those of the finite element method (FEM). The main theory of FDEM involves the algorithms of governing equations, deformation description, contact detection, and contact interaction (Lei et al., 2016; Munjiza et al., 2006).

The general governing equation of the FDEM is (Munjiza, 2004)

$$\mathbf{M}\ddot{\mathbf{x}} + \mathbf{C}\dot{\mathbf{x}} = \mathbf{f}, \tag{1}$$

where $\mathbf{M}$ is the lumped mass matrix, $\mathbf{C}$ is the damping matrix, $\mathbf{x}$ is the displacement vector, and $\mathbf{f}$ is the equivalent force vector acting on each FEM node. This equation solves the dynamic response of a solid material subjected to external forces and satisfies the mass and momentum conservation automatically. An explicit time integration scheme based on a central difference method is employed to solve Eq. (1) with respect to time to obtain the transient evolution of the system. Deformation of finite elements is described by a multiplicative decomposition-based formulation, which allows for a detailed analysis of material deformation (Munjiza et al., 2014). The contact detection between discrete elements is conducted using the MRCK (Munjiza-Rougier-Carney-Knight) algorithm (Rougier and Munjiza, 2010), which determines whether any two given elements, one called the contactor and the other one the target, share at least one search cell. After processing the contact detection, a list that contains all the pairs of elements potentially in contact is established and sent for contact interaction analysis. A penalty function based contact interaction algorithm is used to calculate the contact forces between contacting elements (Munjiza, 2004; Munjiza et al., 2011). Detailed calculation of normal and tangential contact forces is demonstrated in Text S1 of the Supplementary Material.

It is beyond the scope of the present paper to provide a complete description of the above principles; however, details of these can be found in FDEM monographs (Munjiza, 2004; Munjiza et al., 2011, 2014). FDEM allows explicit geometric and mechanical realization of systems involving both continua and discontinua, which makes it superior to both FEM and DEM. Since its inception (Munjiza, 1992), FDEM has proven its computational efficiency and reliability, and has been extensively used in a wide range of endeavors in both industry and academia (Euser et al., 2019; Gao et al., 2018; Lei and Gao, 2018; Lei et al., 2019; Okubo et al., 2019; Rougier et al., 2019). Additionally, benefiting from the recent implementation of a large-strain large-rotation formulation and grand scale parallelization in FDEM by the Los Alamos National Laboratory (Lei et al., 2014; Munjiza et al., 2014), the FDEM software package – HOSS (Hybrid Optimization Software Suite) (Knight et al., 2015; Munjiza et al., 2013) – offers a powerful tool to study the behavior of sheared granular fault system.

2.2. Model setup

Fig. 1a illustrates the geometry of the FDEM model, which is based on the laboratory photoelastic experiment conducted by Geller et al. (2015). The model uses two-dimensional plane stress conditions and consists of 2,817 cylindrical particles confined between two identical deformable plates. The diameter of the particles is either 1.2 or 1.6 mm, and they are randomly placed between the plates. Each plate has dimensions of 570 mm × 250 mm in width and height, respectively. Two stiff bars are attached to the bottom end of the lower plate and to the top end of the upper plate on which the normal load *P* and shear velocity *V* are applied, respectively. At the interfaces between the plates and the particles, fault roughness is simulated as a series of half-circular shaped "teeth" (Fig. 1a). The teeth diameter and the separation between them are 1.6 mm and 0.8 mm, respectively. A number of "sensor" points are set on the centers of both the upper and lower teeth, close to the interface with the gouge, to track the motion of both plates during stick-slips. To avoid edge effects, a portion comprising around 80 mm on both the left and right sides of the gouge are not considered in the plate motion analysis, and thus the information collected from a total of 286 sensors (143 on each plate) is
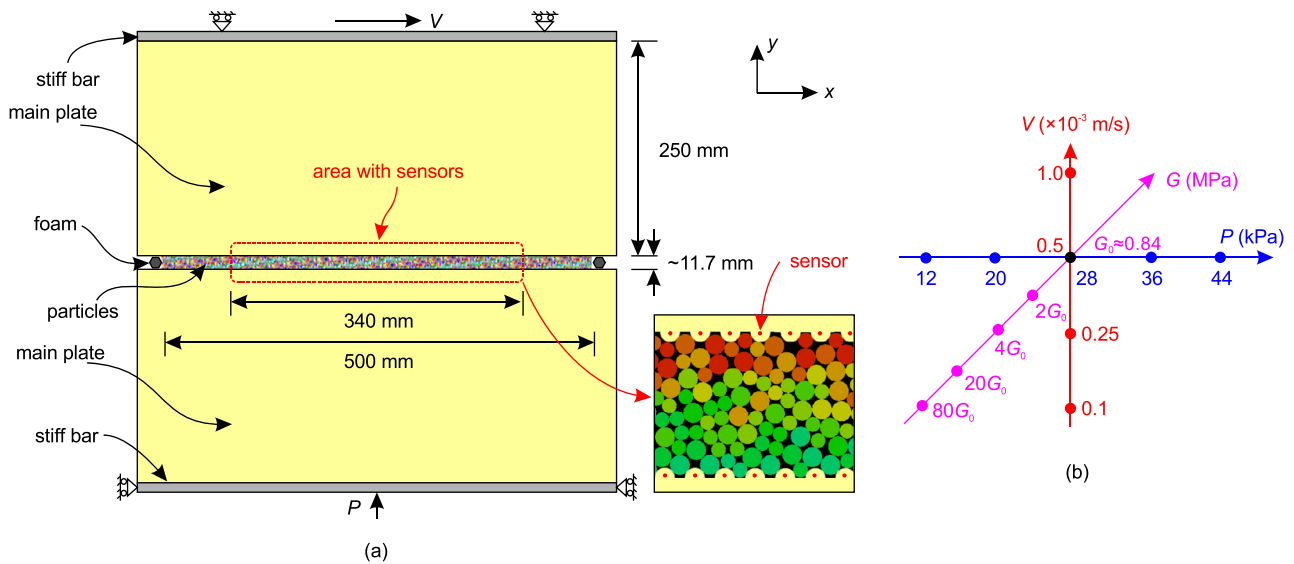
Fig. 1. Model setup and selection of key simulation parameters. (a) FDEM model of the granular fault system and the sensor locations for plate motion monitoring. (b) Illustration of the three groups of models for examining the influence of normal load P (first group, blue), shear velocity V (second group, red) and plate shear modulus G (third group, magenta) on plate motion; the common parameter combination of the three model groups is marked as black at the origin. (For interpretation of the colors in the figure(s), the reader is referred to the web version of this article.)

Table 1
Material and numerical simulation parameters.

Property	Value	Property	Value
Particle diameter	1.2 or 1.6 mm	Stiff bar density	2,800 kg/m^3
Particle density	1,150 kg/m^3	Stiff bar Young's modulus	30 GPa
Particle Young's modulus	0.4 GPa	Stiff bar Poisson's ratio	0.33
Particle Poisson's ratio	0.4	Foam density	1,150 kg/m^3
Particle-particle friction coefficient	0.15	Foam Young's modulus	1 MPa
Number of particles	2,817	Foam Poisson's ratio	0.4
Main plate density	1,150 kg/m^3	Contact penalty	4 GPa
Main plate Poisson's ratio	0.49	Time step	1.0E-4 ms
Particle-plate friction coefficient	0.15		

used in this work. This data collection reflects the dynamic evolution of a section of about 340 mm in length located in the middle of the gouge (Fig. 1a).

The granular fault gouge is consolidated by first moving the top and bottom stiff bars towards each other to ensure the particles are well contacted. After consolidation, the gouge thickness and length are approximately 11.7 mm and 500 mm, respectively. Then the top stiff bar begins shearing, i.e., displacing horizontally towards the right-hand side, with a constant horizontal velocity V, while the normal load P on the bottom stiff bar is held constant throughout the simulation. During the shearing stage, the top stiff bar is allowed to move only in the x-direction and the bottom stiff bar is allowed to move only in the y-direction. The main simulation parameters are tabulated in Table 1, while a detailed illustration of the model geometry and parameter selection is presented in Text S2 of the Supplementary Material. The simulation results were compared and calibrated against the laboratory experiments conducted by Geller et al. (2015) in our previous work (Gao et al., 2018) in which we calculated the laboratory equivalence of seismic moment based on the sensor displacements recorded along the boundary between the shearing plates and fault gouge. The simulations show good agreement with the laboratory results and thus demonstrate the capability and accuracy of FDEM for such simulation.

In the following simulations, a shear velocity $V = 5.0E-4$ m/s is selected first, and for the models with plate Young's modulus $E = 2.5$ MPa (equivalent to a plate shear modulus of $G = G_0 \approx 0.84$ MPa), a series of normal loads P ranging from 12 kPa to 44 kPa

with increments of 8 kPa are used to investigate the influence of normal load on plate motion. Then, to explore the effect of shear velocity, for the models with the same plate shear modulus G_0 and subjected to $P = 28$ kPa, another three shear velocities $V = 1.0E-4$, 2.5E-4 and 1.0E-3 m/s are employed. Finally, for the models subject to $P = 28$ kPa and $V = 5.0E-4$ m/s, four additional plate shear moduli $G = 2G_0$, $4G_0$, $20G_0$ and $80G_0$ (equivalent to plate Young's moduli of $E = 5$, 10, 50 and 200 MPa, respectively) are employed to further examine the influence of plate stiffness on simulation results. Here, we only focus on the effect of normal load, shear velocity and plate stiffness on plate motion, with all other parameters held constant for all models. All combinations of normal load, shear velocity and plate stiffness used here are within the domain that guarantees repetitive stick-slip events. The parameter combinations of the three groups of models are summarized in Fig. 1b.

The simulations use a time step of 1.0E-4 ms, and each model is run for roughly 3.0E+8 time steps with a total shearing time of approximately 30,000 ms. Each model reaches steady state after the first 3,000 ms, approximately. Because of this, in this work, the data for the analysis was collected after 5,000 ms of simulation time. The shear and normal forces between the particles and the upper and lower plates, as well as the x velocity and displacement of the 143 pairs of sensors, are recorded every 1 ms. This time step interval for output recording is chosen carefully through a series of comparisons by considering the resolution of output as well as the computational cost. The particle-plate shear and normal forces are calculated by first resolving the normal and tangential contact forces between each particle-plate contact pair into
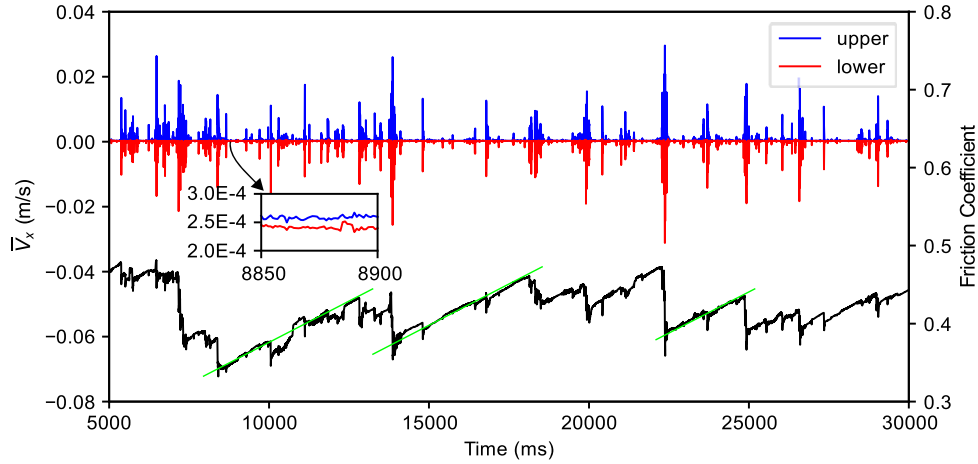
Fig. 2. Comparison between the average x velocity at each output step at locations adjacent to the plate-gouge interfaces, and the plate-gouge macroscopic friction coefficient. Upper panel (left y-axis): time series of average x velocity of the 143 sensors on the upper (blue) and lower (red) plate, respectively; the inset illustrates the average velocity difference between the upper and lower plates during the interevent (stick) phases. Lower panel (right y-axis): time series of macroscopic friction coefficient; the green lines indicate the approximately constant slope of the macroscopic friction coefficient during the interevent time.

x and y directions and then integrating them respectively along the particle-plate interfaces. The ratio of the shear to normal force is then calculated as the macroscopic friction coefficient between the plates and granular fault gouge.

3. Simulation results

3.1. General characteristics of plate motion

The x velocities at the 143 sensor points on each of the upper and lower plate are averaged at each output step (every 1 ms). The time series of the averages for the model with the common parameter combination indicated by the black dot at the origin in Fig. 1b (i.e., $P = 28$ kPa, $V = 5.0E-4$ m/s, and $G = G_0 \approx 0.84$ MPa) are presented in Fig. 2. The average x velocity of the upper plate sensors exhibits primarily positive values, whereas the lower plate sensors generally exhibit the opposite motions (i.e., the upper and lower x velocities are anti-correlated). To facilitate analysis between the plate motion and the stick-slips in the granular fault system, we also plot in Fig. 2 the change of gouge-plate macroscopic friction coefficient with respect to time. During stick phases, the macroscopic friction coefficient increases in an approximately linear manner. At the end of a stick phase, a rapid drop of macroscopic friction coefficient, which marks a slip event, can be observed. The temporal variations of both the upper and lower plate average x velocities match well with the gouge-plate macroscopic friction coefficient. When slip occurs, because of the partial contact loss between plates and particles, the bottom portion of the upper plate lurches to the right and the top portion of the lower plate resets towards its original position to the left. As a result, the upper and lower gouge-plate interfaces have a simultaneous sudden increase of x velocity magnitude but in opposite directions. Particularly, large x velocity magnitudes are generally associated with large macroscopic friction coefficient drops. Additionally, the average x velocities of the upper and lower plate sensors with respect to time are nearly symmetric, manifested by a spike at the bottom of the upper plate towards the right, attended by a spike of similar magnitude at the top of the lower plate toward the left. Whereas during the stick phases, a gradual increase of macroscopic friction coefficient is regularly accompanied with a constant average x velocity around 2.5E-4 m/s (half of the shear velocity V) in the direction of shear for both upper and lower plates (see inset of Fig. 2). All other models exhibit sim-

ilar characteristics regarding the x velocity in both stick and slip phases.

To further interpret plate motion, we examine the average x displacements ($\bar{D}_x$) of the 143 upper and 143 lower plate sensors at each output step, and their time series are presented in Fig. 3a. The average x displacements of upper plate sensors move from 0 to 13.5 mm approximately uniformly in time with an average velocity $\bar{V} \approx 13.5/27000 = 5.0E-4$ m/s, which is equal to the driving shear velocity V on the upper plate. The average x displacements of the lower plate sensors are $x = 0$, i.e., the lower plate does not on average move. During stick phases, the upper and lower plates are locked and move together with a velocity of $V/2$. During slip time, the top of the lower plate retreats to $x \approx 0$ and the bottom of the upper plate lurches to a new position atop the lower plate. The upper and lower plates are then locked anew and repeat the stick-slip cycle, as is demonstrated in the cartoon in Fig. 3b. In the following two sections, we give a detailed analysis of the plate motion in terms of x velocities at the sensors in slip and stick phases, respectively, and investigate how they are influenced by the normal load, shear velocity and plate stiffness.

3.2. Plate motion during slip phases

Because the x velocities of the upper and lower plate sensors during slip phases have almost the same magnitudes but occur in opposite directions, we use a "couple velocity" of each corresponding upper and lower sensor pair to explore the plate motion by considering the trends of both velocities along the gouge-plate interfaces. The x couple velocity for each sensor pair in a specific output time step is defined as

$$V_{x_i}^C = \frac{V_{x_i}^U - V_{x_i}^L}{2}, \tag{2}$$

where the superscripts "C", "U" and "L" denote "couple", "upper" and "lower", respectively, and $i = 1, 2, \ldots 143$ is the sensor number counted from left to right along the gouge for both the upper and lower plates. Since here we focus on plate motions during slip phases, only $V_x^C \geq 1.0E-3$ m/s are considered. The complementary cumulative distribution functions (CCDFs) of V_x^C for the three groups of models are presented in Fig. 4. The CCDF gives the probability of an x couple velocity larger than or equal to a certain magnitude, and thus provides a useful tool for comparing the influence of different parameters on the frequency and magnitude
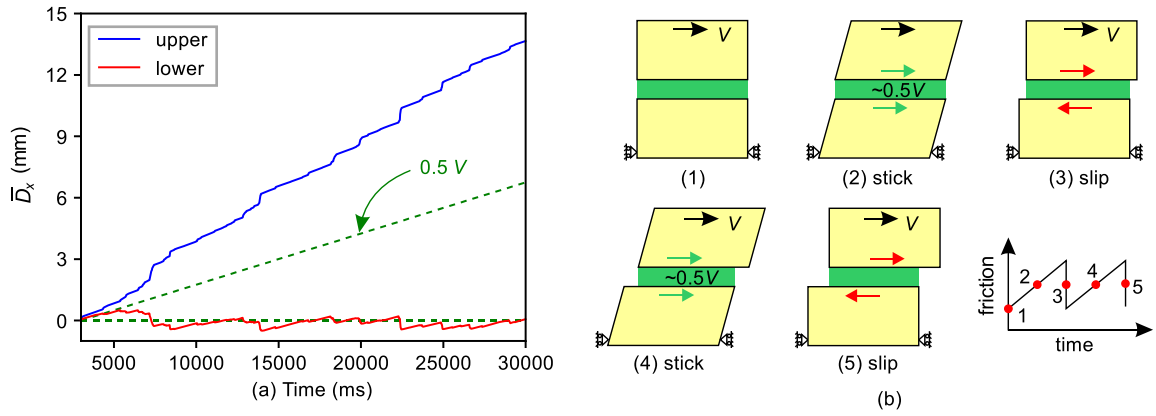
Fig. 3. (a) Time series of average x displacement of the 143 sensors on the upper (blue) and lower (red) plate, respectively; the two green auxiliary dotted lines indicate that the displacements having zero and $V/2$ velocities, respectively. (b) Cartoon illustration of plate motion during stick and slip phases.
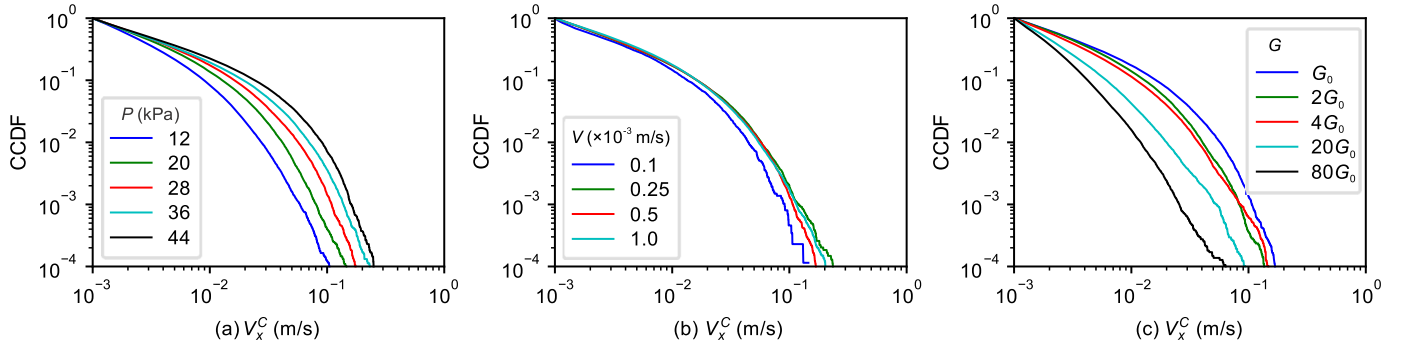

Fig. 4. Complementary cumulative distribution functions (CCDFs) of the x couple velocity during slip phases for the (a) first, (b) second and (c) third group of models shown in Fig. 1b.

of slip events, especially on the large ones. As can be seen from Fig. 4, the largest x velocities of the three groups of models are approximately located around 0.1 m/s, and could be as large as 2-3 orders of the shear velocity. As the normal load increases, larger V_x^C is generated, which indicates that the system is more responsive during slips when subjected to higher normal loads (Fig. 4a). The change of shear velocity seems to have no significant influence on the plate motion along the gouge-plate interfaces during slip phases, as is manifested by the nearly overlapping CCDFs in Fig. 4b. However, stiffer plates suppress local vibrations and result in a relatively "quiet" system with smaller x velocity magnitudes during slip (Fig. 4c).

The x couple velocity correlates well with the drop of macroscopic friction coefficient. To compare the two, we first calculate the mean of the 143 x couple velocities at each output step, and then for the time intervals during slip events we calculate the drop of macroscopic friction coefficient and also average the calculated mean couple velocities for adjacent output time steps. The results are plotted in the top row of Fig. 5, which demonstrates that the magnitude of macroscopic friction coefficient drop generally increases with the increasing x couple velocity. Moreover, the changing ratio between the macroscopic friction coefficient drop and x couple velocity (i.e., the slope of the fitted lines in Fig. 5) increases with the decreasing normal load (Fig. 5a). In other words, for the models with smaller normal loads, the same magnitude of slip could induce a larger macroscopic friction coefficient drop when compared with the models under larger normal loads. Similar trends can be found for the models with larger shear velocities (Fig. 5b, although relatively small) and stiffer plates (Fig. 5c).

To better demonstrate the scale of macroscopic friction coefficient drop and to facilitate comparison, we also plot in the bottom row of Fig. 5 their CCDFs for the three model groups. The macro-

scopic friction coefficient drop increases approximately with the decreasing normal load as well as the increasing shear velocity and plate stiffness. We suspect this may due to the characteristics of our model: the plates are significantly softer than the particles. When subjected to the prescribed normal loads, apparent deformations on the plates along the gouge-plate boundary will occur, and thus result in a series of well-contacted areas at each contact point between the plate and particles. Particularly, for the models subjected to larger normal loads, when slip occurs it will be difficult for these well-contacted points to fully lose contact. While for models subjected to smaller normal loads, some contact points along the gouge-plate boundary may easily lose contact, and thus yield a larger drop of macroscopic friction coefficient when compared with the larger normal load models (Fig. 5d). Although, here, the influence of normal load on friction coefficient drop is not very distinct. For a similar reason, in terms of the plate stiffness, relatively small contact areas will occur at each contact point along the gouge-plate boundary when stiffer plates are employed, and thus when slip occurs, larger friction coefficient drops could be observed (Fig. 5f). Furthermore, large shear velocity weakens the contacts between the plate and particles and will yield a more significant friction coefficient drop during slip phases (Fig. 5e).

3.3. Plate motion during stick phases and interpretation of gouge effective shear modulus

To examine the plate motion during stick phases, we first plot in Fig. 6a the probability density functions (PDFs) of all the output x velocities of the 143 sensor points on each of the upper and lower plates for the model with the common parameter combinations indicated by the black dots shown in Fig. 1b. The markers with the same color as the line represent the corresponding max-
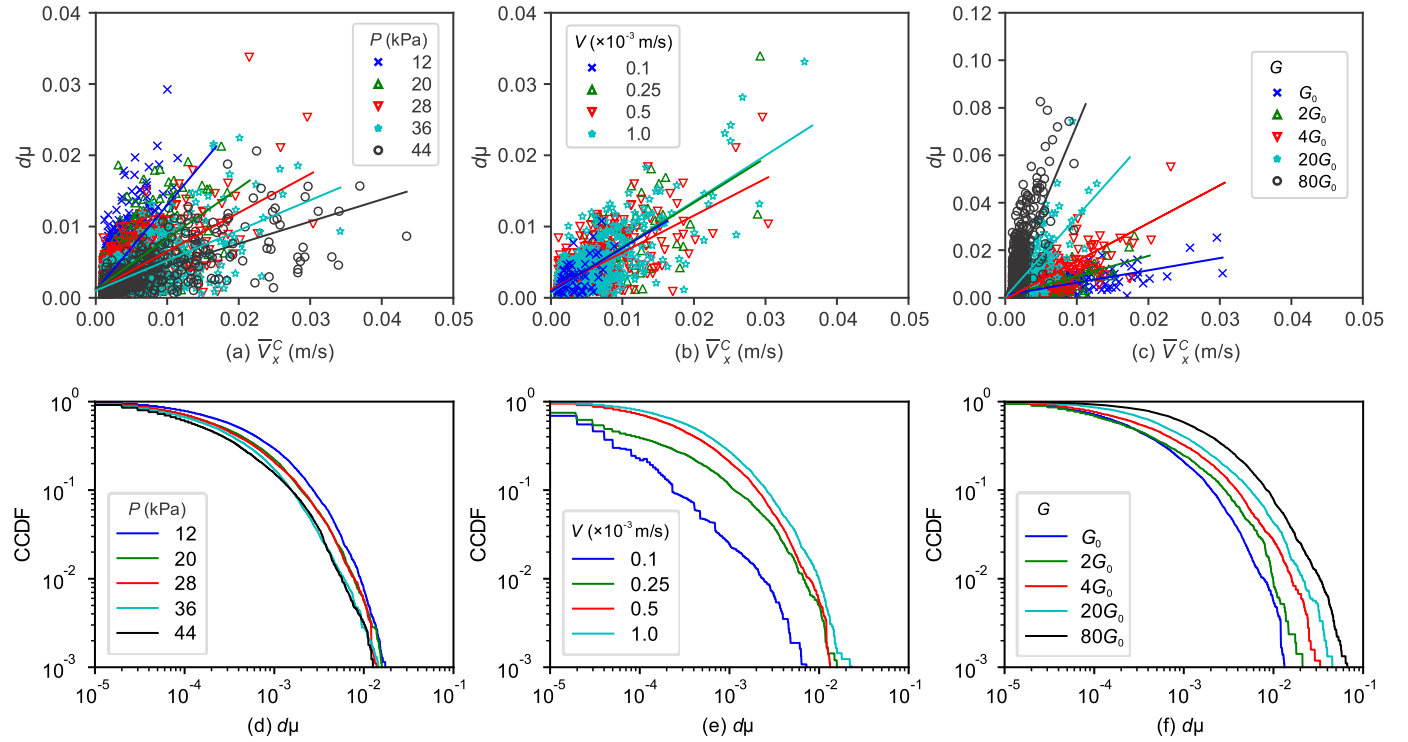
Fig. 5. Top row: Relationship between the drop of macroscopic friction coefficient and the corresponding *x* couple velocity for the (a) first, (b) second and (c) third group of models demonstrated in Fig. 1b; the lines are linear fits between the friction coefficient drop and the *x* couple velocity to facilitate comparison. Bottom row: Complementary cumulative distribution functions (CCDFs) of the macroscopic friction coefficient drop during slips for the (d) first, (e) second and (f) third group of models.

imum and minimum *x* velocities. As can be seen from Fig. 6a, the *x* velocities have both positive and negative values, and positive velocities with large magnitude are mainly seen on the upper plate, while negative velocities with large magnitude mostly occur on the lower plate. This is consistent with the signs of average *x* velocities shown in Fig. 2. The *x* velocities of the sensors on both plates are highly concentrated around 2.5E-4 m/s (i.e., *V*/2, see inset of Fig. 6a), and the modes of PDFs shown in the inset reflect plate motions during the stick phases. A quick comparison reveals that during the stick phases, the upper plate sensor *x* velocities are slightly greater than *V*/2 and the lower plate sensor *x* velocities are slightly less than *V*/2, which is in response to the average *x* velocity difference between the two plates shown in the inset of Fig. 2. This *x* velocity difference is evidence that the gouge is experiencing a growing shear strain necessary to support the growing shear stress in the system. Specifically, during stick phases the shear stress in the system is growing steadily (as indicated in Fig. 2), and the gouge must support the growing shear stress; it does so by developing a growing shear strain, i.e., the upper plate in places adjacent to the gouge moves slightly faster than that of the lower plate. The plate motions of other models, shown in Figs. S3-S5 in the Supplementary Material, manifest similar characteristics.

The velocity difference between the upper and lower plate sensors, i.e.,

$$dV_x^S = V_x^{U'} - V_x^{L'},\qquad(3)$$

indicates the rate of shear strain growth across the gouge, where the superscript "*S*" denotes "stick", and $V_x^{U'}$ and $V_x^{L'}$ represent the upper and lower plate *x* velocity during stick phases (i.e., the modes of PDFs of *x* velocities shown in Fig. 6a), respectively. We calculate dV_x^S for the three groups of models and the results are presented in Fig. 6b-d: dV_x^S decreases with the increasing normal

load, and increases with the increasing shear velocity and plate shear modulus. The shear strain rate can be further calculated by

$$\dot{\gamma} = \frac{d\gamma}{dt} = \frac{dV_x^S}{\bar{H}},\qquad(4)$$

where $\bar{H}$ is the average gouge thickness in each model, and here $\bar{H} \approx 11.7$ mm. As can be interpreted from Fig. 6b-d, large normal loads suppress the shear strain rate, which reveals that during stick phases the gouge is more compact and the upper and lower plates are moving in a more synchronized fashion (i.e., smaller relative velocity difference) when the system is compressed by larger normal loads. However, a faster shear velocity increases the relative velocity difference between the upper and lower plates and thus yields a larger shear strain rate. When the shear plates are stiffer, deformation is limited inside the plates and thus, the bottom part of the upper plate moves in an almost similar manner as the top part in which the constant shear velocity is enforced; since the bottom part of the lower plate is fixed in the *x*-direction, more sliding and particle rolling will occur during the shear and thus a larger shear strain rate is generated. Particularly, the plate stiffness has higher notable influence on the shear strain rate than the normal load and shear velocity, as is demonstrated by the larger dV_x^S in Fig. 6d when compared with Fig. 6b & c.

Additionally, as mentioned earlier and indicated by the green lines in Fig. 2, the macroscopic friction coefficient between the gouge and plates also increases at an approximately uniform rate in time. This indicates the shear stress rate applied on the gouge, as we have

$$\dot{\tau} = \frac{d\tau}{dt} = P\frac{d\mu}{dt},\qquad(5)$$

where τ is the shear stress between gouge and plates and μ is the macroscopic friction coefficient. Thus, we obtain the effective shear modulus of the gouge for each model in an approximation manner using
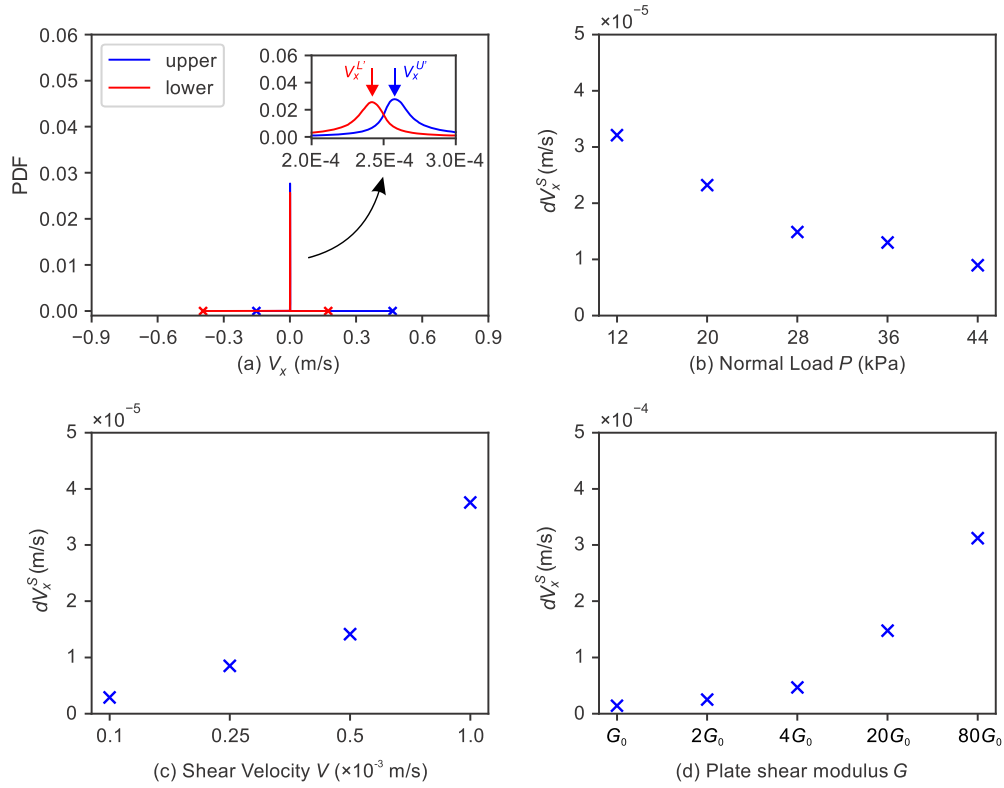
Fig. 6. Analyses of x velocity of the 143 sensor pairs during stick phases. (a) Probability density functions of all output x velocities of the 143 sensor pairs on the upper and lower plate, respectively, for the model with the common parameter combination of normal load, shear velocity and plate shear modulus shown in Fig. 1b; the markers with the same color as the line represent the corresponding maximum and minimum values. The velocity difference between the upper and lower plates during stick phases for the (a) first, (b) second and (c) third group of models demonstrated in Fig. 1b.
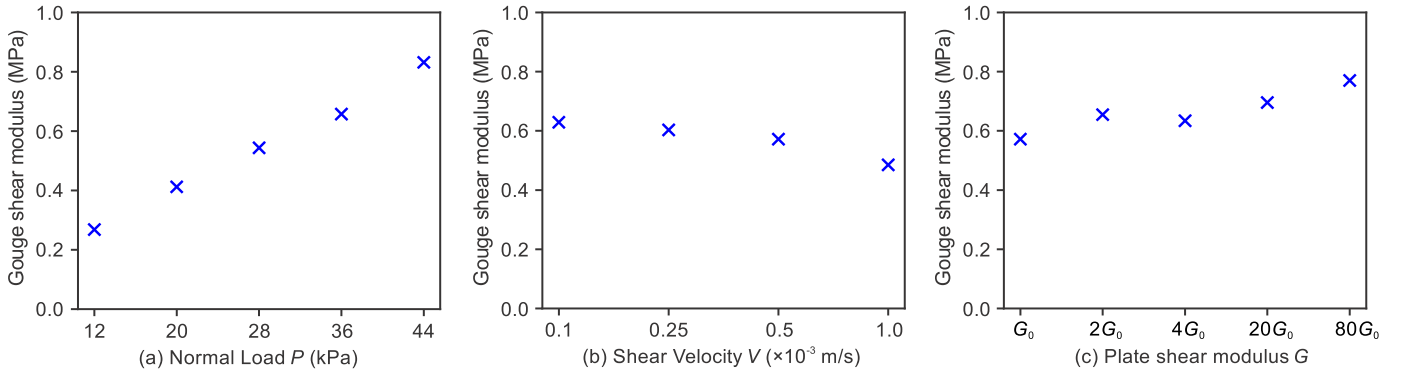

Fig. 7. Gouge effective shear modulus of the (a) first, (b) second and (c) third group of models demonstrated in Fig. 1b.

$$G = \frac{d\tau}{d\gamma} = \frac{\dot{\tau}}{\dot{\gamma}}. \tag{6}$$

Although the granular gouge may not behave in an exact elastic manner during the stick phases (as indicated by the small friction drops in Fig. 2), here, the calculated effective gouge shear modulus reflects the mechanical behavior of the gouge under different normal load, shear velocity and plate shear modulus. The gouge effective shear moduli of the three groups of models are calculated and presented in Fig. 7. These effective shear moduli are generally within the range between 0.2 and 0.9 MPa. The increasing normal load enhances the effective shear modulus of the granular gouge (Fig. 7a). While the gouge effective shear modulus reduces when subjected to larger shear velocity (Fig. 7b). A stiffer shear plate could increase the gouge effective shear modulus (Fig. 7c). All these may be attributed to the influence of normal load, shear velocity and plate shear modulus on the stress chain distributions

inside the granular gouge (Gao et al., 2019). Specifically, a larger normal load intensifies the stress chain force formed by adjacent particle interactions and thus increases the gouge effective shear modulus. Likewise, a stiffer shearing plate can more effectively transfer the external normal load to the gouge and strengthen particle contacts. However, a faster shear velocity may weaken the stress chain network and reduce the gouge effective shear modulus. Furthermore, the effective shear modulus increases approximately linearly with the increasing normal load, e.g., a nearly four times increase of normal load (from 12 kPa to 44 kPa) results in a roughly four times rise of gouge effective shear modulus (Fig. 7a). When compared with the normal load, the effect of shear velocity and plate shear modulus on gouge effective shear modulus is less significant. For instance, a ten-times increase of shear velocity only results in a less than 10% reduction of gouge shear modulus, and
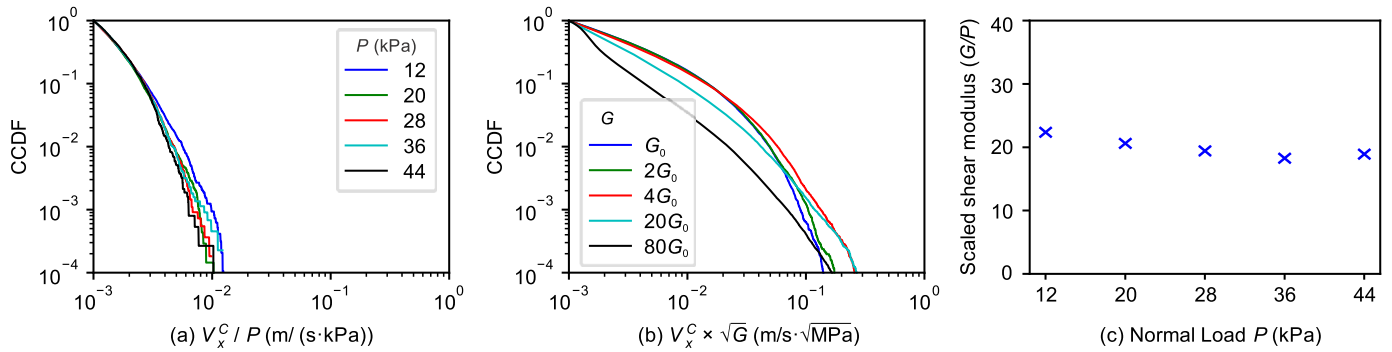
Fig. 8. Scaling of the results related to plate motion in stick and slip phases: scaling of CCDFs of the x couple velocity during slips for the (a) first, (b) third group of models; (c) scaling of gouge effective shear modulus for the first group of models.

similarly, the gouge effective shear modulus only witnesses 10% increases when the plate stiffness is increased by 80 times.

4. Discussion

In summary, the two main characteristics derived here, i.e., the x couple velocity which represents the plate motion during slip phases and the gouge effective shear modulus interpreted from the motion of the plates during stick phases, may be significant for revealing the fault mechanics. As discussed above, these two characteristics are influenced by the normal loads, shear velocities and plate stiffness. First, we find that for the first group of models, after dividing the x couple velocity at slips by the corresponding normal load, the resulting CCDFs collapse upon one other (Fig. 8a). This reveals that the plate motion during slip phases is proportional to the normal load acting on the system. For the second group of models, the four shear velocities do not have a very distinct influence on the plate motion during slips (see Fig. 4b). Regarding the influence of different plate shear modulus, we found that the CCDFs of the x couple velocity of the third group of models multiplied by $\sqrt{G}$ seems reasonably close (Fig. 8b). This indicates that the plate motion during slip phases may be inversely proportional to the square root of plate shear modulus.

Similar to the effect of normal load on plate motion during slip phases, the gouge effective shear modulus also scales with the normal load (Fig. 8c), i.e., the gouge shear modulus increases proportionally with the normal load. Therefore, we suspect that the geometrical structures of stress chains that carrying forces are similar for all models with different normal loads, and expect the spectrum of stresses to have amplitudes controlled by the normal load. This needs further detailed investigation; however, although the shear velocity and plate stiffness do influence the gouge stiffness, e.g., larger shear velocity could weaken the gouge effective shear modulus and a stiffer plate may enhance the gouge effective shear modulus, their influence is minor, especially when compared with the influence of normal load. Through the above analyses, we speculate that the normal load determines the structure of elastic elements in the gouge that give the system its frictional properties. In other words, the normal load determines the nature and strength of the stress chains. Whereas the shear velocity and plate stiffness are the driving system which determines the rate at which the elastic elements in the gouge have their strength tested.

It is worth mentioning that the trend of plate motion (indicated by x couple velocity here) with respect to normal load and plate stiffness are consistent with those discussed in the existing literature (e.g., Lapusta and Rice, 2003; Rice, 1983; Rubin and Ampuero, 2005; Ruina, 1983; Scuderi et al., 2017b), i.e., the plate motion increases with increasing normal load and decreasing plate shear modulus. However, the friction coefficient drop shows the opposite trends to the existing literature. Unfortunately, the exact reason

is not clear at the moment. Additionally, in the current analysis, only the influence of normal load, shear velocity and plate stiffness on plate motion is discussed. However, other parameters such as gouge thickness, particle-particle and particle-plate friction coefficient, particle size distribution and the presence of fluids may also play significant roles in the behavior of elastic elements in the gouge that give the system its frictional properties. Further work is necessary to provide a thorough characterization of the above remaining problems.

5. Conclusions

We have applied the FDEM to explicitly simulate the stick-slip induced near gouge plate motion in a sheared granular gouge fault system. In the FDEM model, the plates and particles are represented by discrete elements to track their motion and interaction with neighboring objects, and each discrete element is further discretized into finite elements to capture its deformation during shear loads. Three groups of models with a total of 12 simulations have been conducted to respectively explore the influence of normal load, shear velocity and plate stiffness on the plate motion in terms of x velocity and x displacement in locations adjacent to the gouge during the stick and slip phases. The gouge effective shear modulus is also interpreted based on the plate motion, and a potential scaling of plate motion and the gouge effective shear modulus with respect to normal load, shear velocity and plate stiffness is discussed.

The simulations show that for all the models, during each slip event, the bottom of the upper plate lurches to the right and the top of the lower plate resets towards the left. The x couple velocity for each sensor pair on the upper and lower plates is used to analyze the plate motion during slip events. The results indicate that the maximum x velocities could be as large as 2-3 orders of the shear velocity. As the normal load increases, larger x couple velocities are generated. The shear velocity seems to have no significant influence on plate motion during slips, while stiffer plates result in a relatively "quieter" system with smaller x velocity magnitudes. The x couple velocity correlates well with the drop of macroscopic friction coefficient, and large x velocity magnitudes are generally associated with large macroscopic friction coefficient drops. For the models subjected to smaller normal loads, the same x couple velocity can cause larger drops of macroscopic friction coefficient. Large friction drops during slips can also be more frequently observed when using stiffer plates. However, the shear velocity seems to have no distinct effect on the correlation between macroscopic friction coefficient drop and x couple velocity.

During the stick phases, the x velocities recorded at the sensors located on the upper and lower plate are respectively slightly greater and slightly less than half of the shear velocity. This small x velocity difference between the upper and lower plates is evidence

that the gouge is experiencing a growing shear strain necessary to support the growing shear stress in the system. We have calculated both the shear strain and shear stress rates for all the models and thus obtained the gouge effective shear modulus. The results show that both the increasing normal load and plate stiffness enhance the effective shear modulus of the gouge, while larger shear velocity has the opposite effect. However, compared with the normal load, the effect of shear velocity and plate shear modulus on gouge effective shear modulus is less significant.

The scaling analysis shows that the x velocity at slips is proportional to the normal load acting on the system. The shear velocity does not show a distinct influence on the plate motion during slip phases. The x velocity at slips may be inversely proportional to the square root of the plate shear modulus. Additionally, the gouge effective shear modulus increases proportionally with the normal load, while the influence of shear velocity and plate shear modulus on gouge effective shear modulus is minor when compared with the normal load. We suspect that the normal load determines the nature and strength of the stress chains that mainly control the frictional properties of the gouge. Whereas the shear velocity and plate stiffness only determine the rate at which the elastic elements in the gouge have their strength tested. The simulations disclose the influence of normal load, shear velocity and fault block stiffness on the stick-slip induced near gouge vibration, and may help understand the complex behavior of earthquake source physics and dynamics.

Declaration of competing interest

The authors state that there are no known conflicts of interest associated with this publication and there was no financial support for this work that could have influenced its outcome.

Acknowledgements

Appendix A. Supplementary material

Supplementary material related to this article can be found online at https://doi.org/10.1016/j.epsl.2020.116481.

References

Abe, S., Mair, K., 2005. Grain fracture in 3D numerical simulations of granular shear. Geophys. Res. Lett. 32. https://doi.org/10.1029/2004GL022123.

de Arcangelis, L., Ciamarra, M.P., Lippiello, E., Godano, C., 2011. Micromechanics and statistics of slipping events in a granular seismic fault model. J. Phys. Conf. Ser. 319, 012001.

Dorostkar, O., Guyer, R.A., Johnson, P.A., Marone, C., Carmeliet, J., 2017a. On the micromechanics of slip events in sheared, fluid-saturated fault gouge. Geophys. Res. Lett. 44, 6101–6108. https://doi.org/10.1002/2017GL073768.

Dorostkar, O., Guyer, R.A., Johnson, P.A., Marone, C., Carmeliet, J., 2017b. On the role of fluids in stick-slip dynamics of saturated granular fault gouge using a coupled computational fluid dynamics-discrete element approach. J. Geophys. Res., Solid Earth 122, 3689–3700. https://doi.org/10.1002/2017JB014099.

Dratt, M., Katterfeld, A., 2017. Coupling of FEM and DEM simulations to consider dynamic deformations under particle load. Granul. Matter 19, 49. https://doi.org/10.1007/s10035-017-0728-3.

Euser, B., Rougier, E., Lei, Z., Knight, E.E., Frash, L.P., Carey, J.W., Viswanathan, H., Munjiza, A., 2019. Simulation of fracture coalescence in granite via the combined finite–discrete element method. Rock Mech. Rock Eng. 52, 3213–3227. https://doi.org/10.1007/s00603-019-01773-0.

Ferdowsi, B., Griffa, M., Guyer, R.A., Johnson, P.A., Marone, C., Carmeliet, J., 2013. Microslips as precursors of large slip events in the stick-slip dynamics of sheared granular layers: a discrete element model analysis. Geophys. Res. Lett. 40, 4194–4198. https://doi.org/10.1002/grl.50813.

Ferdowsi, B., Griffa, M., Guyer, R.A., Johnson, P.A., Marone, C., Carmeliet, J., 2014. Three-dimensional discrete element modeling of triggered slip in sheared granular media. Phys. Rev. E 89, 042204.

Gao, K., Euser, B.J., Rougier, E., Guyer, R.A., Lei, Z., Knight, E.E., Carmeliet, J., Johnson, P.A., 2018. Modeling of stick-slip behavior in sheared granular fault gouge using the combined finite-discrete element method. J. Geophys. Res., Solid Earth 123, 5774–5792. https://doi.org/10.1029/2018JB015668.

Gao, K., Guyer, R., Rougier, E., Ren, C.X., Johnson, P.A., 2019. From stress chains to acoustic emission. Phys. Rev. Lett. 123, 048003. https://doi.org/10.1103/PhysRevLett.123.048003.

Geller, D.A., Ecke, R.E., Dahmen, K.A., Backhaus, S., 2015. Stick-slip behavior in a continuum-granular experiment. Phys. Rev. E 92, 060201.

Griffa, M., Daub, E.G., Guyer, R.A., Johnson, P.A., Marone, C., Carmeliet, J., 2011. Vibration-induced slip in sheared granular layers and the micromechanics of dynamic earthquake triggering. Europhys. Lett. 96, 14001.

Griffa, M., Ferdowsi, B., Guyer, R.A., Daub, E.G., Johnson, P.A., Marone, C., Carmeliet, J., 2013. Influence of vibration amplitude on dynamic triggering of slip in sheared granular layers. Phys. Rev. E 87, 012205.

Jackson, J., McKenzie, D., 1988. The relationship between plate motions and seismic moment tensors, and the rates of active deformation in the Mediterranean and Middle East. Geophys. J. Int. 93, 45–73. https://doi.org/10.1111/j.1365-246X.1988.tb01387.x.

Johnson, P.A., Ferdowsi, B., Kaproth, B.M., Scuderi, M., Griffa, M., Carmeliet, J., Guyer, R.A., Le Bas, P.Y., Trugman, D.T., Marone, C., 2013. Acoustic emission and microslip precursors to stick-slip failure in sheared granular material. Geophys. Res. Lett. 40, 5627–5631. https://doi.org/10.1002/2013GL057848.

Johnson, P.A., Jia, X., 2005. Nonlinear dynamics, granular media and dynamic earthquake triggering. Nature 437, 871–874.

Johnson, P.A., Savage, H., Knuth, M., Gomberg, J., Marone, C., 2008. Effects of acoustic waves on stick-slip in granular media and implications for earthquakes. Nature 451, 57–60.

Knight, E.E., Rougier, E., Lei, Z., 2015. Hybrid optimization software suite (HOSS) – educational version. Technical Report. Los Alamos National Laboratory, Los Alamos National Laboratory.

Lapusta, N., Rice, J.R., 2003. Nucleation and early seismic propagation of small and large events in a crustal earthquake model. J. Geophys. Res., Solid Earth 108. https://doi.org/10.1029/2001jb000793.

Lei, Q., Gao, K., 2018. Correlation between fracture network properties and stress variability in geological media. Geophys. Res. Lett. 45, 3994–4006. https://doi.org/10.1002/2018GL077548.

Lei, Z., Rougier, E., Knight, E.E., Munjiza, A., 2014. A framework for grand scale parallelization of the combined finite discrete element method in 2d. Comput. Part. Mech. 1, 307–319. https://doi.org/10.1007/s40571-014-0026-3.

Lei, Z., Rougier, E., Knight, E.E., Munjiza, A.A., Viswanathan, H., 2016. A generalized anisotropic deformation formulation for geomaterials. Comput. Part. Mech. 3, 215–228. https://doi.org/10.1007/s40571-015-0079-y.

Lei, Z., Rougier, E., Munjiza, A., Viswanathan, H., Knight, E.E., 2019. Simulation of discrete cracks driven by nearly incompressible fluid via 2D combined finite-discrete element method. Int. J. Numer. Anal. Met. 43, 1724–1743. https://doi.org/10.1002/nag.2929.

Ma, G., Zhou, W., Chang, X.-L., Chen, M.-X., 2016. A hybrid approach for modeling of breakable granular materials using combined finite-discrete element method. Granul. Matter 18, 7. https://doi.org/10.1007/s10035-016-0615-3.

Mair, K., Abe, S., 2008. 3D numerical simulations of fault gouge evolution during shear: grain size reduction and strain localization. Earth Planet. Sci. Lett. 274, 72–81. https://doi.org/10.1016/j.epsl.2008.07.010.

Mair, K., Hazzard, J.F., 2007. Nature of stress accommodation in sheared granular material: insights from 3D numerical modeling. Earth Planet. Sci. Lett. 259, 469–485. https://doi.org/10.1016/j.epsl.2007.05.006.

Marone, C., 1998. The effect of loading rate on static friction and the rate of fault healing during the earthquake cycle. Nature 391, 69–72.

Marone, C., Raleigh, C.B., Scholz, C.H., 1990. Frictional behavior and constitutive modeling of simulated fault gouge. J. Geophys. Res., Solid Earth 95, 7007–7025. https://doi.org/10.1029/JB095iB05p07007.

Munjiza, A., Rougier, E., John, N.W.M., 2006. MR linear contact detection algorithm. Int. J. Numer. Methods Eng. 66, 46–71. https://doi.org/10.1002/nme.1538.

Munjiza, A.A., 1992. Discrete Elements in Transient Dynamics of Fractured Media. Swansea University.

Munjiza, A.A., 2004. The Combined Finite-Discrete Element Method. John Wiley & Sons.

Munjiza, A.A., Knight, E.E., Rougier, E., 2011. Computational Mechanics of Discontinua. John Wiley & Sons.

Munjiza, A.A., Rougier, E., Knight, E.E., 2014. Large Strain Finite Element Method: A Practical Course. John Wiley & Sons.

Munjiza, A.A., Rougier, E., Knight, E.E., Lei, Z., 2013. HOSS: an integrated platform for discontinua simulations. In: Chen, G., Ohnishi, Y., Zheng, L., Sasaki, T. (Eds.), Frontiers of Discontinuous Numerical Methods and Practical Simulations in Engineering and Disaster Prevention. CRC Press, pp. 97–104.

Okubo, K., Bhat, H.S., Rougier, E., Marty, S., Schubnel, A., Lei, Z., Knight, E.E., Klinger, Y., 2019. Dynamics, radiation and overall energy budget of earthquake rupture

with coseismic off-fault damage. J. Geophys. Res., Solid Earth. https://doi.org/10.1029/2019jb017304.

Rice, J.R., 1983. Constitutive relations for fault slip and earthquake instabilities. Pure Appl. Geophys. 121, 443–475. https://doi.org/10.1007/BF02590151.

Rivière, J., Lv, Z., Johnson, P.A., Marone, C., 2018. Evolution of b-value during the seismic cycle: insights from laboratory experiments on simulated faults. Earth Planet. Sci. Lett. 482, 407–413. https://doi.org/10.1016/j.epsl.2017.11.036.

Rouet-Leduc, B., Hulbert, C., Bolton, D.C., Ren, C.X., Riviere, J., Marone, C., Guyer, R.A., Johnson, P.A., 2018. Estimating fault friction from seismic signals in the laboratory. Geophys. Res. Lett. 45, 1321–1329. https://doi.org/10.1002/2017GL076708.

Rouet-Leduc, B., Hulbert, C., Lubbers, N., Barros, K., Humphreys, C.J., Johnson, P.A., 2017. Machine learning predicts laboratory earthquakes. Geophys. Res. Lett. 44, 9276–9282. https://doi.org/10.1002/2017GL074677.

Rougier, E., Munjiza, A., Lei, Z., Chau, V.T., Knight, E.E., Hunter, A., Srinivasan, G., 2019. The combined plastic and discrete fracture deformation framework for FDEM. Int. J. Numer. Methods Eng. https://doi.org/10.1002/nme.6255.

Rougier, E., Munjiza, A.A., 2010. MRCK_3D contact detection algorithm. In: Proceedings of 5th International Conference on Discrete Element Methods. London, UK.

Rubin, A.M., Ampuero, J.-P., 2005. Earthquake nucleation on (aging) rate and state faults. J. Geophys. Res., Solid Earth 110. https://doi.org/10.1029/2005jb003686.

Ruina, A., 1983. Slip instability and state variable friction laws. J. Geophys. Res., Solid Earth 88, 10359–10370. https://doi.org/10.1029/JB088iB12p10359.

Scuderi, M.M., Collettini, C., Marone, C., 2017a. Frictional stability and earthquake triggering during fluid pressure stimulation of an experimental fault. Earth Planet. Sci. Lett. 477, 84–96. https://doi.org/10.1016/j.epsl.2017.08.009.

Scuderi, M.M., Collettini, C., Viti, C., Tinti, E., Marone, C., 2017b. Evolution of shear fabric in granular fault gouge from stable sliding to stick slip and implications for fault slip mode. Geology 45, 731–734. https://doi.org/10.1130/g39033.1.

Siman-Tov, S., Brodsky, E.E., 2018. Gravity-independent grain size segregation in experimental granular shear flows as a mechanism of layer formation. Geophys. Res. Lett. 45, 8136–8144. https://doi.org/10.1029/2018gl078486.

Taylor, S.E., Brodsky, E.E., 2019. Energy partitioning in granular flow depends on mineralogy via nanoscale plastic work. J. Geophys. Res., Solid Earth 124, 6397–6408. https://doi.org/10.1029/2019jb017762.

Wang, C., Elsworth, D., Fang, Y., 2017. Influence of weakening minerals on ensemble strength and slip stability of faults. J. Geophys. Res., Solid Earth 122, 7090–7110. https://doi.org/10.1002/2016JB013687.